Check for updates

MXene/graphene oxide heterojunction as a high performance anode material for lithium ion batteries

Li Wang,[a] Kun Yuan,[b] Hongyu Bai,[c] Ping Xuan,[d] Na Xu,[d] Chaofan Yin,[a] Kechen Li,[b] Pengju Hao,[b] Yang Zhou [ID] *[b] and Binbin Dong [ID] *[a]

MXene/graphene oxide composites with strong interfacial interactions were constructed by ball milling in vacuum. Graphene oxide (GO) acted as a bridge between $Ti_3C_2T_x$ nanosheets in the composite material, which could buffer the mechanical shear force during the ball milling process, avoid the structural damage of nanosheets and improve the structural stability of the composite material during the lithium process. Partial oxidation of $Ti_3C_2T_x$ nanosheets is caused by high temperatures during ball milling, which is beneficial to improve the intercalation of lithium ions in the material, reduce the stress and electrostatic repulsion between adjacent layers, and cause the composite to have better lithium storage performance. Under the high current density of 2.5 A g^{-1}, the reversible capacity of the $Ti_3C_2T_x$/GO composite material after 2000 cycles was 116.5 mA h g^{-1}, and the capacity retention was as high as 116.6%.

1. Introduction

With the development of portable electronic devices and electric vehicles, lithium-ion batteries became a research hotspot because of their high energy density, lack of memory effect and wide operating voltage window. $Ti_3C_2T_x$ has the advantages of adjustable layer spacing, abundant surface functional groups and multiple active sites, which had unique advantages in the field of lithium-ion battery electrode materials. However, the layer spacing decreased due to the van der Waals attraction between the layers, which seriously hindered the penetration of electrolyte, reducing the rapid migration of lithium ions, and affecting the electrochemical performance.[1,2]

In order to further improve the lithium storage performance of $Ti_3C_2T_x$, one of the most promising strategies was to combine $Ti_3C_2T_x$ nanosheets with other nanomaterials to form heterogeneous structures.[3,4] At present, many materials such as transition metal oxides (TMOs),[5–7] transition metal sulphides (TMDCs),[8,9] phosphorus,[10,11] silicon,[12,13] polymers,[14,15] and carbon materials[16–19] are loaded between $Ti_3C_2T_x$ nanosheets, which could increase the ion transport rate and buffer the volume expansion of the nanoparticles, and ensure the fast

charge transport in the heterojunction materials. The existence of a $Ti_3C_2T_x$ nano-sheet layer could avoid the agglomeration of nano-particles, which is beneficial to the effective utilization of surface active sites, thus improving the electrochemical properties of heterojunction composites.

In this paper, the $Ti_3C_2T_x$/GO heterojunction composites were prepared by high-speed ball milling in vacuum. Graphene oxide acted as a spacer between $Ti_3C_2T_x$ nano-layers in order to enlarge the space between them, which increased the charge storage capacity of the composite and promoted the diffusion of electrolyte in the electrode reaction. Moreover, graphene oxide exhibited high conductivity, which contributed to interlayer charge transfer and improved the multiples properties of the composites.

2. Experimental

2.1 Preparation of $Ti_3C_2T_x$ and GO

Graphene oxide (GO) was prepared by the oxidation reaction of graphite powder (99.9% purity, Alfa Aesar, USA) using a modified Hummers' method [18]. H_2SO_4 (12 mL), $K_2S_2O_8$ (2.5 g) and P_2O_5 (2.5 g) were mixed and heated in a flask, and graphite powder (3 g, 325 mesh) was added at 80 °C and kept at this temperature for 4.5 h. After heating, dilute it with 500 mL deionized water and cool it to room temperature naturally. Let it stand for 10 h before removing it. The seed water is drained and filtered to remove residual acid and dried. Subsequently, the product was placed in concentrated sulfuric acid (120 mL) under ice bath conditions and $KMnO_4$ (15 g) was slowly added. After stirring for 2 h, dilute with 250 mL deionized water and continue stirring for 2 h. After that, 700 mL of deionized water

[a]School of Materials Science and Engineering, Henan Province International Joint Laboratory of Materials for Solar Energy Conversion and Lithium Sodium Based Battery, Luoyang Institute of Science and Technology, Luoyang 471023, PR China. E-mail: dongbb@lit.edu.cn

[b]Faculty of Materials Metallurgy and Chemistry Engineering Research Institute, Jiangxi University of Science and Technology, Ganzhou 341000, PR China

[c]Yanshi Zhongyue Refractory Co. LTD, Luoyang 471900, PR China

[d]Anhui Product Quality Supervision & Inspection Research Institute, PR China

was added to dilute the solution, and 20 mL of 30%H_2O_2 was used to neutralize the solution until the color of the mixture turned bright yellow with bubbling. The mixture is then filtered and washed with 10% HCl solution to remove metal ions, and then washed repeatedly with deionized water until the pH value of the filtrate is ∼6. Finally, the precipitate is dried in a freezer to obtain graphene oxide (GO). It was then ball milled at 500 rpm for 12 h to be used as backup for reserve.

The commercial Ti_3AlC_2 powder was purchased from 11 Technology Co., Ltd (Jilin, China). The layered Ti_3AlC_2 was chemically etched to remove the Al layer by wet etching as follows: after 1 g LiF and 20 mL 9 M HCl solution were magnetically stirred in a Teflon beaker for 30 min, 1 g Ti_3AlC_2 powder was slowly added into the above solution, and the etching reaction was carried out for 36 h at 35 °C under magnetic stirring. Subsequently, the precipitation was obtained by centrifugation at 6000 rpm and washed with deionized water several times until the pH value reached ∼6. Then, the sediment was placed in 200 mL 0.25 M LiOH solution, ultrasonic treatment and stirred for 24 h. The alkalized mixture is repeatedly filtered and washed with deionized water until the pH of the solution reaches ∼8. Finally, the precipitate was dried in a freeze-dryer to obtain multilayer $Ti_3C_2T_x$ MXene (multi-Ti3C2T$_x$). Subsequently, $Ti_3C_2T_x$ was obtained by ball milling at 500 rpm for 12 h in a vacuum environment for backup.

2.2 Preparation of $Ti_3C_2T_x$/GO composite

The multi-$Ti_3C_2T_x$ and GO nanosheets were taken in a mass ratio of 9 : 1 and placed in a vacuum environment with mixed ball milling at a speed of 500 rpm for 12 h. After that, by calcination at 300 °C for 3 h under inert atmosphere with a heating rate of 2 °C min^{-1}. The as-prepared product was designated as $Ti_3C_2T_x$/GO. Control the GO content but different composite materials was prepared.

2.3 Electrochemical measurements

As for the lithium-ion battery tests, all of the CR2032-type coin cells were assembled in an Ar-filled glove box. The working electrode was prepared by mixing $Ti_3C_2T_x$ or S–$Ti_3C_2T_x$, acetylene black, and polyvinylidene fluoride (PVDF) in N-methyl-2-pyrrolidinone (NMP) with a weight ratio of 6 : 2 : 2. Lithium foil was used as counter electrode, Celgard polypropylene as separators and 1 M LiPF6 in ethylene carbonate (EC) and dimethyl carbonate (DMC) a volumetric ratio of 1 : 1 as the electrolyte. All electrochemical performance tests were conducted under 25 °C. Cyclic voltammetry experiments were performed by LAND CT2001A battery testing system at a scan rate of 0.1 mV s^{-1} between 0.05 and 3 V. Electrochemical impedance spectroscopy (EIS) measurements were performed using an AC amplitude of 10 mV and a frequency range of 200 kHz to 0.01 Hz.

2.4 Characterization

The morphology and structural information were conducted by SEM (SU-8020, Hitachi) and TEM (JEOL JEM-2100F). The XRD patterns were collected on a Bruker D8 diffractometer (Cu Kα

radiation, $\lambda = 1.5406$ Å). The element surface analysis was carried out by XPS (Axis Ultra DLD, Kratos Analytical) with Al Kα radiation. The specific surface area of the sample was determined by N_2 absorption at 77 K with a BeiShiDe 3H-2000PM1 instrument. The Raman spectra were collected on a Raman spectrometer (Labram-010) using 532 nm laser.

3. Results and discussion

As shown in Fig. 1a, $Ti_3C_2T_x$ presented a typical layered structure after chemical etching, but there was still a serious self-stacking phenomenon. GO had very large horizontal and vertical dimensions, with internal three-dimensional holes connected to each other (Fig. 1b).[20] When the two mixtures were milled and treated at high temperature, the size of the particles was significantly reduced, but the flake graphene was like a ribbon floating between the $Ti_3C_2T_x$ particles (Fig. 1c and d).

In order to deeply analyze the morphological structure of $Ti_3C_2T_x$/GO composites, transmission electron microscopy (TEM) was used for further characterization. According to Fig. 2a and b, it can be clearly seen that GO is coated in the outermost layer of the material, where the lattice spacing of 0.22 nm and 0.35 nm corresponds to $Ti_3C_2T_x$ (103) and TiO_2 (110) crystal planes, respectively. In addition, the interface structure of TiO_2/$Ti_3C_2T_x$ appeared in Fig. 2c and d,[21–23] and there is an obvious lattice fringe interruption phenomenon, which indicated that $Ti_3C_2T_x$ is partially oxidized due to mechanical ball milling and large transverse shear force. The XRD results (Fig. 3a) further confirm the presence of a small amount of TiO_2,[22,24] which was consistent with TEM results. Raman spectra (Fig. 3b) further confirmed the successful recombination of $Ti_3C_2T_x$ and GO. The vibrational peak at 141.9 cm^{-1} in the $Ti_3C_2T_x$/GO composite represented the A_{1g} symmetric out-of-plane vibrations of the titanium atoms in the material, while the vibrational peaks at 417.2 and 692.6 cm^{-1} indicated the in-plane shear vibrations (E_g) of Ti, C and surface oxygen-containing functional groups in the $Ti_3C_2T_x$ material, respectively, where the vibrational peak at 292.3 cm^{-1} peak then verified the production of TiO_2 in the material.[25,26] Meanwhile, the typical peaks of the carbon material were located at 1346.5 and 1599.9 cm^{-1}, corresponding to the D and G peaks of graphene oxide, respectively, indicating the generation of amorphous carbon during the reaction.[25,27] After graphene oxide composite $Ti_3C_2T_x$, the intensity ratio (I_D/I_G) of the two peaks increased from 0.92 to 1.08, indicating that most of the oxygen functional groups on its surface were removed and TiO_2 was directly embedded into the graphene surface, increasing the large number of defects generated and exposing more active sites on the composite surface, which is conducive to increasing the contact area of the electrolyte and promoting the ion and charge diffusion.[28]

In order to analyze the chemical composition and surface electronic states of $Ti_3C_2T_x$/GO composites, XPS spectroscopy was performed, as shown in Fig. 4. In the XPS full spectrum, the addition of GO material resulted in a significant increase in the intensity of the C 1s characteristic peak of the composites, and the increase in the intensity of the O 1s characteristic peak was
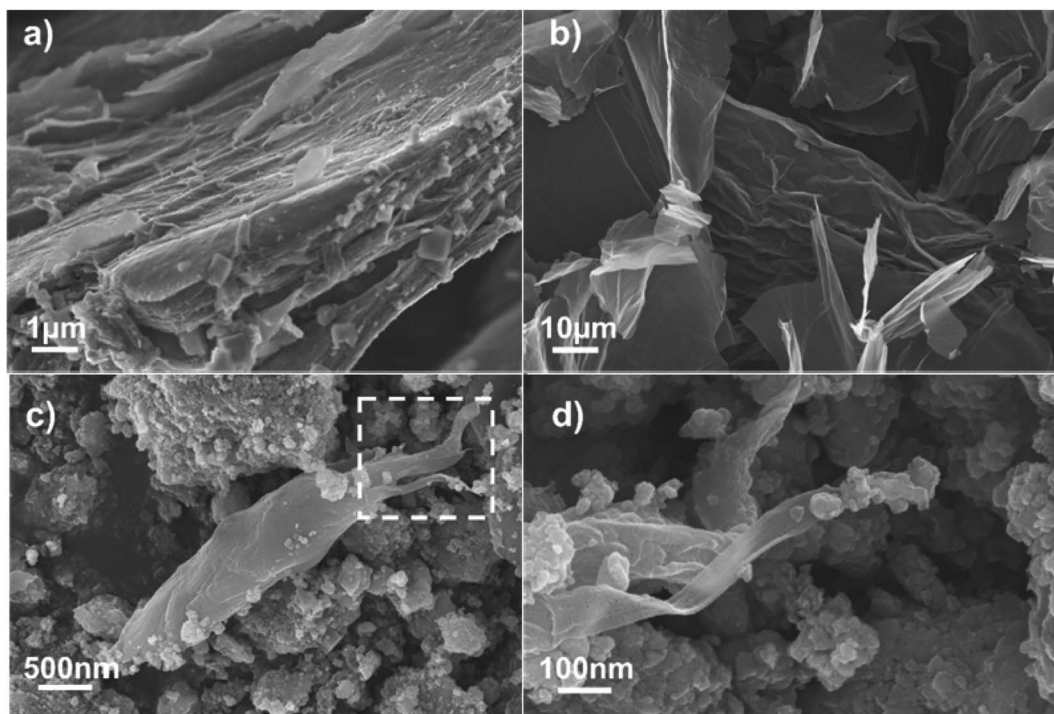
Fig. 1 SEM images of (a) $Ti_3C_2T_x$; (b) GO; (c and d) $Ti_3C_2T_x$/GO composites.
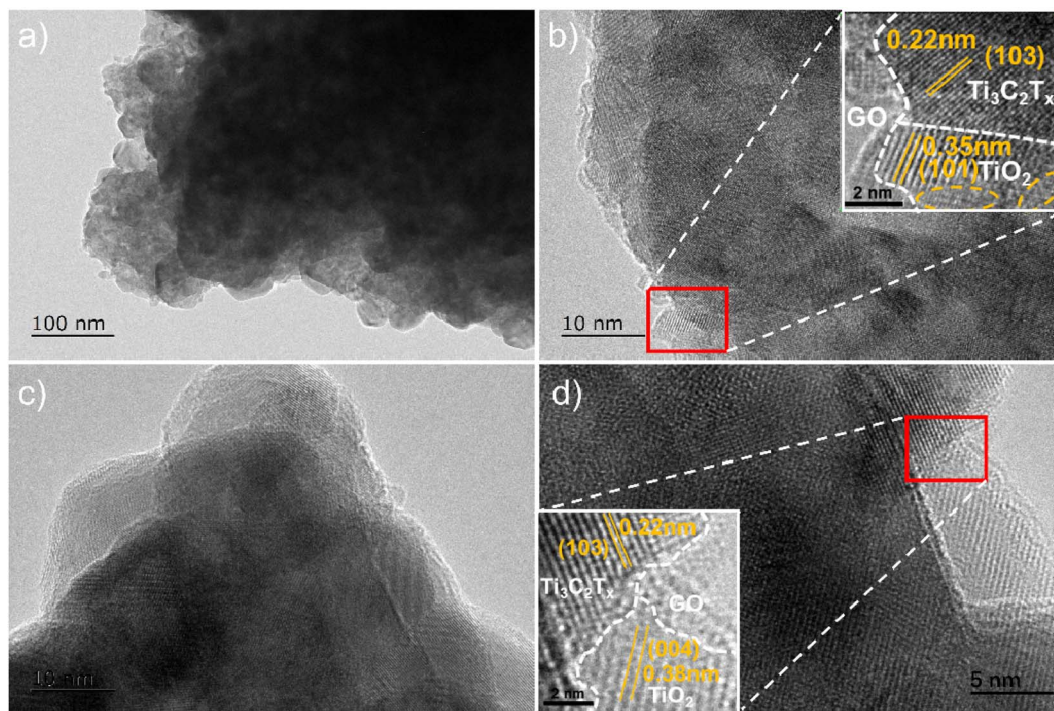
Fig. 2 (a and b) TEM images of $Ti_3C_2T_x$/GO and (c and d) TEM images of TiO_2/$Ti_3C_2T_x$.

attributed to the oxidation of $Ti_3C_2T_x$ nanosheets by high temperature during the ball milling composite. In the XPS high-resolution spectra of Ti 2p orbitals (Fig. 5a and b), there are four distinct characteristic peaks in $Ti_3C_2T_x$. The characteristic peaks at 455.1 and 460.6 eV correspond to Ti(II) ($2p_{3/2}$ and $2p_{1/2}$), 456.6 eV corresponds to Ti(III) ($2p_{3/2}$), while the Ti–C peak at 461.3 eV corresponds to the Ti $2p_{1/2}$ orbital, and the characteristic peaks at 458.5 and 464.3 eV correspond to Ti($2p_{3/2}$ and
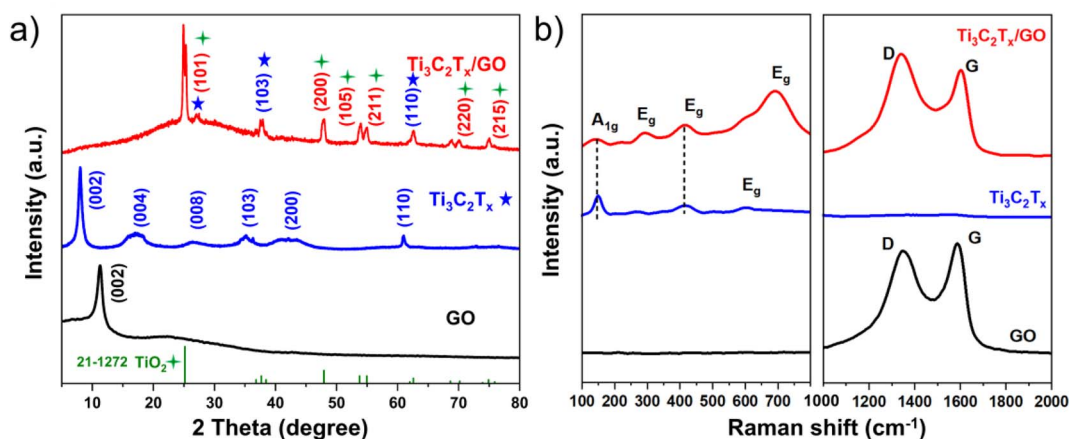
Fig. 3 (a) XRD pattern of GO, $Ti_3C_2T_x$ and $Ti_3C_2T_x$/GO; (b) Raman spectrum.
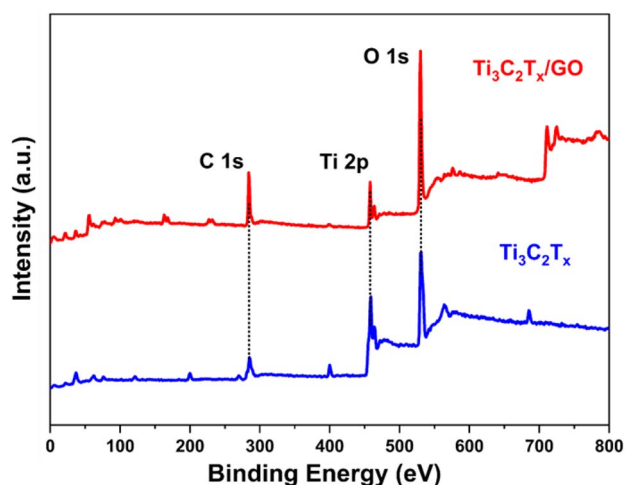
Fig. 4 XPS spectra of $Ti_3C_2T_x$ and $Ti_3C_2T_x$/GO composites.

$2p_{1/2}$).[29,30] After the composite graphene oxide, the characteristic peaks on the Ti 2p orbitals show a significant change and the Ti–C intensity in the structure is weak, which is still mainly due to the generation of TiO_2 in the material and is wrapped by the graphene oxide on its surface along with $Ti_3C_2T_x$. As shown in Fig. 5c and d), the main characteristic peaks present in the C 1s are C–C (284.8 eV), C–O (286.2 eV), C–Ti–O (282.2 eV) and O–C=O (288.8 eV), and the intensity of the C–C peak in the composite was significantly higher than the other characteristic peaks, which then indicated the presence of a large number of C–C bonds in it, which could be attributed to the graphene oxide. Fig. 5e and f) showed the O 1s high-resolution spectra of $Ti_3C_2T_x$, $Ti_3C_2T_x$/GO composites with characteristic peaks corresponding to Ti–O (530.1 eV), C–Ti–(OH)$_x$ (531.2 eV) and O=C–OH (533.2 eV), respectively, where O was mainly present in $Ti_3C_2T_x$ materials in the form of Ti–O bonds, followed in the form of oxygen-containing functional groups on the surface of $Ti_3C_2T_x$, while in the composites, the residual oxygen functional groups of GO caused a slight increase in the peak intensity.

$Ti_3C_2T_x$/GO composite was used as working electrode and lithium sheet as paired electrode to investigate its electrochemical properties in lithium-ion battery. In the voltage range of 0.05–3.0 V, the CV curve of the $Ti_3C_2T_x$/GO composite at sweep velocity of 0.1 mV s^{-1} is shown in Fig. 6a). At 0.99 V, the irreversible peak appeared on the first discharge curve, which was mainly due to the formation of SEI film on the electrode surface and the irreversible reaction between lithium ion and the functional groups on the material surface. In the subsequent cycle, redox peaks at 0.68 V and 1.7 V correspond to lithium ion intercalation/desorption by the following mechanisms:[26,31]

$$Ti_3C_2T_x + y Li + y e^- \leftrightarrow Ti_3C_2T_x Li_y \qquad (1-1)$$
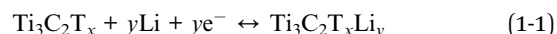
The good overlap of the CV curves in the 3rd and 4th circles then indicated that the $Ti_3C_2T_x$/GO composite has excellent cycling stability in the electrochemical lithium storage process. Fig. 6b shows the charge/discharge curves of the $Ti_3C_2T_x$/GO composite electrode at a current density of 0.1 A g^{-1}, which could correspond well with the CV curves with initial charge/discharge specific capacities of 506.1 and 814.6 mA h g^{-1}, respectively, and a first Coulomb efficiency of 62.13%, due to the presence of abundant functional groups on the surfaces of GO and $Ti_3C_2T_x$ nanosheets that the hybrid ball milling of GO and $Ti_3C_2T_x$ nanosheets exposed a large number of active sites at the same time as reducing their corresponding sizes, increasing their lithium storage capacity. The subsequent overlap of charge/discharge curves also confirmed the more excellent cycling stability of $Ti_3C_2T_x$/GO composites.[32]

After ball milling, the reduction of material particle size shortened the diffusion path of ions and charges and promoted the penetration of electrolyte, which made $Ti_3C_2T_x$/GO exhibit a more excellent multiplicative performance than $Ti_3C_2T_x$, as shown in Fig. 6c. The reversible specific capacities of $Ti_3C_2T_x$/GO reached 275.6, 210.1, 172.8, 147.2, and 130.8 mA h g^{-1} at current densities of 0.5, 1.0, 1.5, 2.0, and 2.5 A g^{-1}, respectively, and the specific capacities at each current density were much
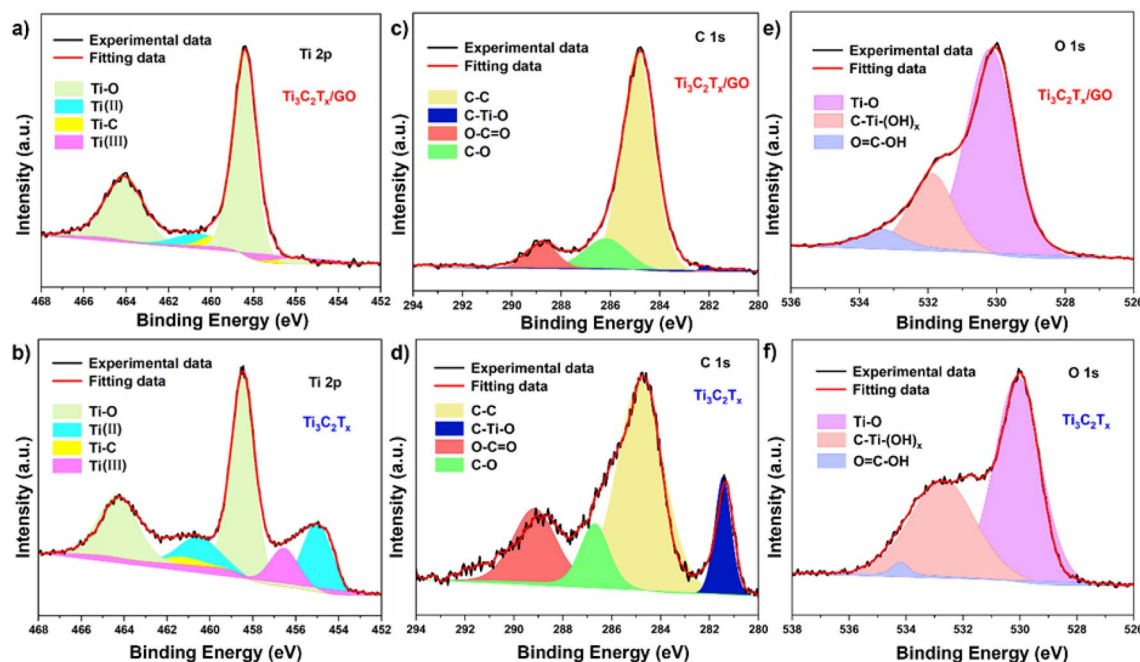
Fig. 5 High resolution XPS spectra of Ti$_3$C$_2$T$_x$/GO and Ti$_3$C$_2$T$_x$: (a and b) Ti 2p; (c and d) C 1s; (e and f) O 1s.
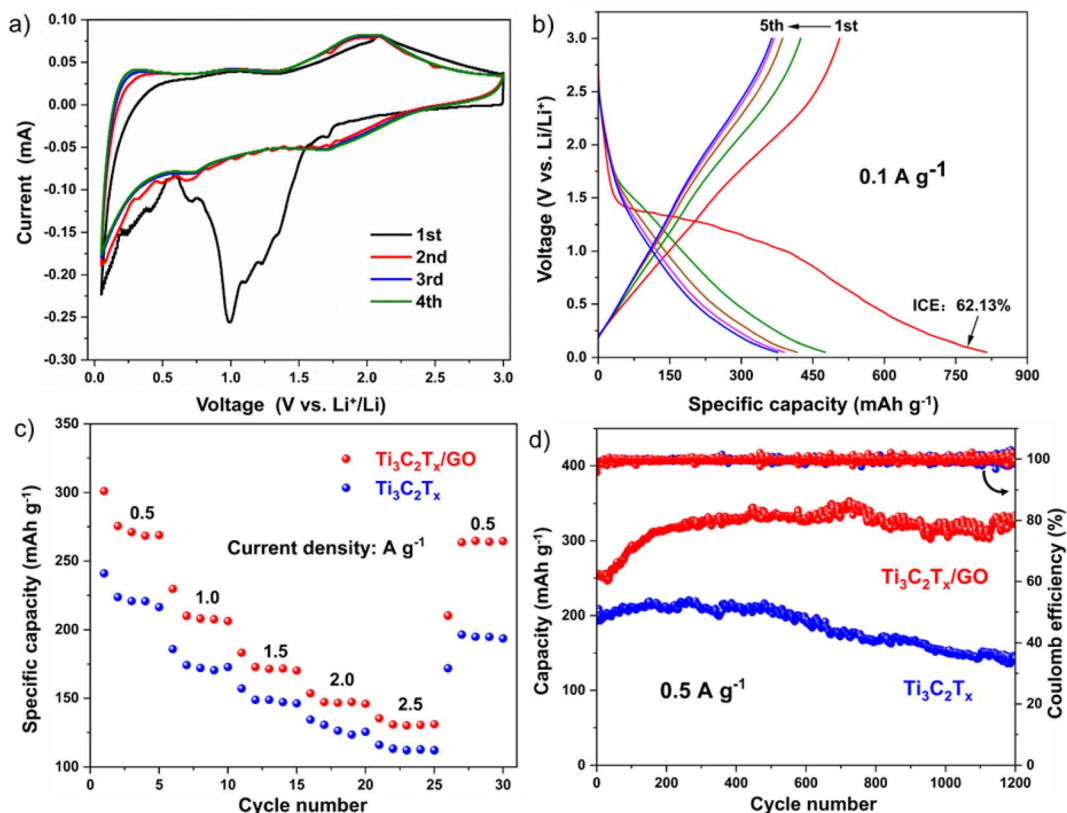
Fig. 6 (a and b) CV curve and charge–discharge curve of Ti$_3$C$_2$T$_x$/GO composites; (c and d) Ti$_3$C$_2$T$_x$ and Ti$_3$C$_2$T$_x$/GO composites multiplier properties and cycle properties.

larger than those of the Ti$_3$C$_2$T$_x$ material after ball milling alone. When the current density was reduced to 0.5 A g^{-1}, Ti$_3$C$_2$T$_x$/GO could recover to a reversible specific capacity of

263.6 mA h g^{-1}, showing excellent reversibility. Subsequently, Ti$_3$C$_2$T$_x$/GO as well as Ti$_3$C$_2$T$_x$ materials were tested for 1200 cycles of performance, as shown in Fig. 6d. At a current density

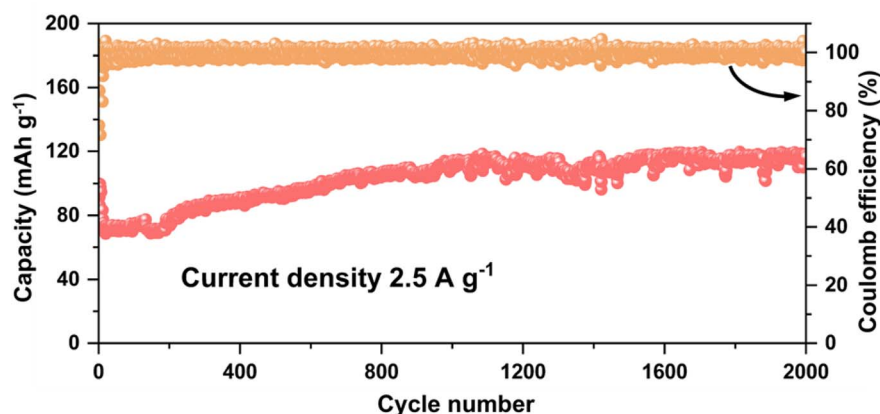**Fig. 7** Long cycle performance of $Ti_3C_2T_x$/GO composites at 2.5 A g^{-1} current density.

of 0.5 A g^{-1}, the specific capacity of $Ti_3C_2T_x$/GO was much higher than that of $Ti_3C_2T_x$. During the first 500 cycles, the electrolyte continuously penetrated between the active particles and the lithium ions were de-embedded several times, which enabled the exposure of more surface active sites, resulting in a gradual increase in the lithium storage capacity of both. However, the capacity of $Ti_3C_2T_x$ materials decayed afterwards, mainly due to the small size of the particles after ball milling,

which prompted the agglomeration of small particles under the continuous embedding of lithium ions and impeded the wetting of the electrolyte, and the irreversible SEI film on the surface of the particles, which seriously affected the rapid ion and charge transport, and the internal lithium storage sites were not fully utilized, resulting in the decay of their capacity.[28] However, graphene oxide in $Ti_3C_2T_x$/GO composites, due to its unique ribbon structure, played a bridging role in it, prompting
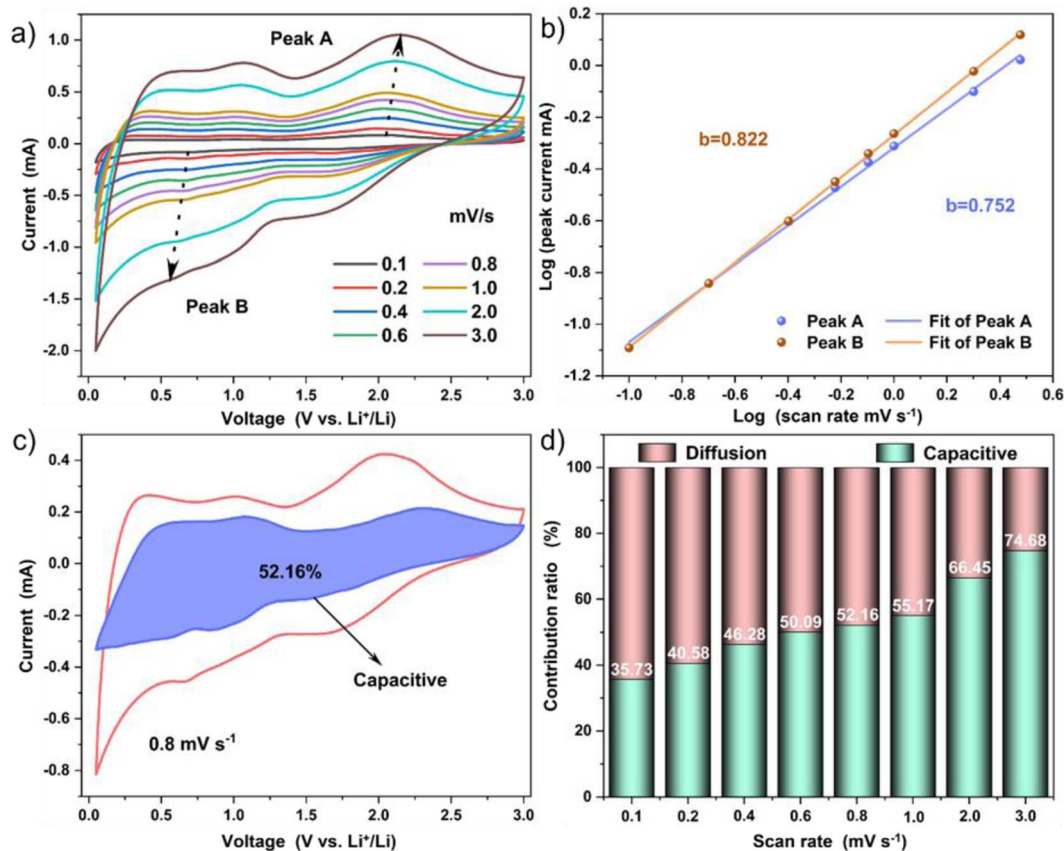

Fig. 8 (a) CV results of $Ti_3C_2T_x$/GO composites at various scan rates from 0.1 to 3 mV s^{-1}. (b) Relationship between the log(peak current i) and log(scan rate ν). (c) CV curve with corresponding capacitive contribution of the $Ti_3C_2T_x$/GO composites at a scan rate of 0.8 mV s^{-1}. (d) Contribution ratio of the capacitive and diffusion-controlled charge storage at various scan rates.

the activation process of the material to continuously expose the active sites and utilize them effectively, showing extremely excellent cycling stability. Then, the $Ti_3C_2T_x$/GO composite was further tested for long cycles at a high current density of 2.5 A g^{-1}, as shown in Fig. 7. The specific capacity of $Ti_3C_2T_x$/GO composite after 2000 cycles was 116.5 mA h g^{-1}, with a capacity retention rate of 116.6%, which fully indicated that the $Ti_3C_2T_x$/GO composite retained good structural stability and had excellent cycling performance after graphene oxide composite. It has excellent cycling performance.

In order to further investigate the electrochemical behavior of $Ti_3C_2T_x$/GO composites, the CV curves of different sweep rates were analyzed accordingly (Fig. 8a). Based on the formula $i = av^b$, where a is a constant and the value of b can be determined by the slope of the $\log(v) - \log(i)$ curve. From the fitting curve of Fig. 8b, the b values of reduction peak and oxidation peak are 0.752 and 0.822, respectively. In contrast, diffusion-controlled embedding mechanism and surface pseudocapacitance mechanism coexist in $Ti_3C_2T_x$/GO electrodes, but the surface-induced pseudo-capacitance process still dominated. In addition, the capacitance contribution ratio of the two reaction mechanisms could be calculated by the following formula:[14,33] $i(v) = k_1v + k_2v^{1/2}$, where $i(v)$, k_1v, $k_2v^{1/2}$ and v are the current, capacitive current, diffusion control current and scanning rate at a given voltage, respectively. According to the CV curve, when the scanning rate is 0.8 mV s^{-1}, the pseudo-capacitance contribution of $Ti_3C_2T_x$/GO electrode is 52.16%. With the increase in scanning rate, the corresponding pseudo-capacitance contribution also increased (Fig. 8c and d). This showed that in the process of charge and discharge, the mechanical ball milling led to a sharp decrease in the particle size of the material, shortening the ion and charge diffusion path, coupled with the good electrical conductivity of graphene oxide and $Ti_3C_2T_x$ nanosheets, which made the charge transfer process in the surface of $Ti_3C_2T_x$/GO composites in a dominant position.[34]

4. Conclusion

$Ti_3C_2T_x$ nanosheets and GO were ball milled in vacuum by high energy ball mill self-assembly method. $Ti_3C_2T_x$/GO composites with strong interfacial interaction could be constructed by forming chemical bonds between the abundant functional groups on the surface of GO and $Ti_3C_2T_x$, which could effectively promote the transport of ions and electrons at the heterogeneous interface and improve its electrochemical behavior. The specific capacity of $Ti_3C_2T_x$/GO composite electrode could reach 506.1 mA h g^{-1} at the current density of 0.1 A g^{-1}, and the reversible capacity of $Ti_3C_2T_x$/GO composite electrode after 2000 cycles is 116.5 mA h g^{-1} at the high current density of 2.5 A g^{-1}. The capacity retention rate is as high as 116.6%.

Conflicts of interest

There are no conflicts to declare.

References

1 W. Nie, H. Cheng, Q. Sun, *et al.*, Design strategies toward high-performance zn metal anode, *Small Methods*, 2023, 2201572.

2 Q. Sun, H. Cheng, Y. Yuan, *et al.*, Uncovering the fundamental role of interlayer water in charge storage for bilayered $V_2O_5 \cdot nH_2O$ xerogel cathode materials, *Adv. Energy Mater.*, 2023, **13**(3), 2202515.

3 D. Xiong, X. Li, Z. Bai, *et al.*, Recent advances in layered $Ti_3C_2T_x$ MXene for electrochemical energy storage, *Small*, 2018, **14**(17), e1703419.

4 Y. Zhang, L. Tao, C. Xie, *et al.*, Defect engineering on electrode materials for rechargeable batteries, *Adv. Mater.*, 2020, **32**(7), e1905923.

5 Q. Chen, Z. Wen, J. Zhang, *et al.*, Fe_3O_4 nanorods in N-doped carbon matrix with pseudo-capacitive behaviors as an excellent anode for subzero lithium-ion batteries, *J. Alloys Compd.*, 2018, **772**, 557–564.

6 X. Li, J. Zhu, Y. Fang, *et al.*, Hydrothermal preparation of CoO/Ti_3C_2 composite material for lithium-ion batteries with enhanced electrochemical performance, *J. Electroanal. Chem.*, 2018, **817**, 1–8.

7 B. Ahmed, D. Anjum, Y. Gogotsi, *et al.*, Atomic layer deposition of SnO_2 on MXene for Li-ion battery anodes, *Nano Energy*, 2017, **34**, 249–256.

8 S. Zhang, H. Ying, P. Huang, *et al.*, Rational design of pillared $SnS/Ti_3C_2T_x$ MXene for superior lithium-ion storage, *ACS Nano*, 2020, **14**(12), 17665–17674.

9 H. Liu, Y. He, H. Zhang, *et al.*, Heterostructure engineering of ultrathin $SnS_2/Ti_3C_2T_x$ nanosheets for high-performance potassium-ion batteries, *J. Colloid Interface Sci.*, 2021, **606**(1), 167–176.

10 H. Liu, S. Zhang, Q. Zhu, *et al.*, Fluffy carbon-coated redphorus as a highly stable and high-rate anode for lithium-ion batteries, *J. Mater. Chem. A*, 2019, **7**(18), 11205–11213.

11 S. Zhang, H. Liu, B. Cao, *et al.*, An MXene/CNTs@P nanohybrid with stable Ti-O-P bonds for enhanced lithium ion storage, *J. Mater. Chem. A*, 2019, **7**(38), 21766–21773.

12 G. Tritsaris, K. Zhao, O. Okeke, *et al.*, Diffusion of lithium in bulk amorphous silicon: a theoretical study, *J. Phys. Chem. C*, 2012, **116**(42), 22212–22216.

13 M. Xia, B. Chen, F. Gu, *et al.*, $Ti_3C_2T_x$ MXene nanosheets as a robust and conductive tight on Si anodes significantly enhance electrochemical lithium storage performance, *ACS Nano*, 2020, **14**(4), 5111–5120.

14 X. Xie, M. Zhao, B. Anasori, *et al.*, Porous heterostructured MXene/carbon nanotube composite paper with high volumetric capacity for sodium-based energy storage devices, *Nano Energy*, 2016, **26**, 513–523.

15 C. Chen, M. Boota, X. Xie, *et al.*, Charge transfer induced polymerization of EDOT confined between 2D titanium carbide layers, *J. Mater. Chem. A*, 2017, **5**(11), 5260–5265.

16 C. Zhang, X. Wang, W. Wei, *et al.*, Recent advances in the synthesis and energy applications of 2D MXenes, *ChemElectroChem*, 2021, **8**(20), 3804–3826.

17 M. Lu, W. Han, H. Li, *et al.*, Tent-pitching-inspired high-valence period 3-cation pre-intercalation excels for anode of 2D titanium carbide (MXene) with high Li storage capacity, *Energy Storage Mater.*, 2019, **16**, 163–168.

18 K. Yuan, P. Hao, X. Hu, J. Zhang and Y. Zhou, Experimental and computational studies on S-decorated Ti_3C_2 MXene as anode material in Li-ion batteries, *J. Mater. Sci.*, 2022, **57**(13), 7001–7011.

19 K. Yuan, P. Hao, Y. Zhou, X. Hu, J. Zhang and S. Zhong, A two-dimensional MXene/BN van der Waals heterostructure as an anode material for lithium-ion batteries, *Phys. Chem. Chem. Phys.*, 2022, **24**(22), 13713–13719.

20 M. Yoo and H. Park, Effect of hydrogen peroxide on properties of graphene oxide in Hummers method, *Carbon*, 2019, **141**, 515–522.

21 Y. Zhang, Y. Tang, W. Li, *et al.*, Nanostructured TiO_2-based anode materials for high-performance rechargeable lithium-ion batteries, *ChemNanoMat*, 2016, **2**(8), 764–775.

22 C. Guo, Q. Tian and L. Yang, The size-controllable spindle TiO_2 nanograins and their lithium storage properties, *J. Alloys Compd.*, 2018, **776**, 740–745.

23 Z. Liu, R. Guo, F. Li, *et al.*, Reduced graphene oxide bridged, TiO_2 modified and MnO_4 intercalated $Ti_3C_2T_x$ sandwich-like nanocomposite as a high performance anode for enhanced lithium storage applications, *J. Alloys Compd.*, 2018, **762**, 643–652.

24 H. Ren, J. Sun, R. Yu, *et al.*, Controllable synthesis of mesostructures from TiO_2 hollow to porous nanospheres with superior rate performance for lithium ion batteries, *Chem. Sci.*, 2015, **7**(1), 793–798.

25 Z. Li, G. Chen, J. Deng, *et al.*, Creating sandwich-like Ti_3C_2/TiO_2/rGO as anode materials with high energy and power density for Li-ion hybrid capacitors, *ACS Sustain. Chem. Eng.*, 2019, **7**(18), 15394–15403.

26 J. Huang, R. Meng, L. Zu, *et al.*, Sandwich-like $Na_{0.23}TiO_2$ nanobelt/Ti_3C_2 MXene composites from a scalable in situ transformation reaction for long-life high-rate lithium/sodium-ion batteries, *Nano Energy*, 2018, **46**, 20–28.

27 C. Shen, L. Wang, A. Zhou, *et al.*, Synthesis and electrochemical properties of two-dimensional RGO/$Ti_3C_2T_x$ nanocomposites, *Nanomaterials*, 2018, **8**(2), 80.

28 Y. Zhang, L. Tao, C. Xie, *et al.*, Defect engineering on electrode materials for rechargeable batteries, *Adv. Mater.*, 2020, **32**(7), e1905923.

29 C. Zhang, S. Kim, M. Ghidiu, *et al.*, Layered orthorhombic Nb_2O_5@$Nb_4C_3T_x$ and TiO_2@$Ti_3C_2T_x$ hierarchical composites for high performance Li-ion batteries, *Adv. Funct. Mater.*, 2016, **26**(23), 4143–4151.

30 L. Jia, Y. Li, L. Su, *et al.*, TiO_2 nanoparticles in situ formed on Ti_3C_2 nanosheets by a one-step ethanol-thermal method for enhanced reversible lithium-ion storage, *Chemistryselect*, 2020, **5**(10), 3124–3129.

31 C. Yang, Y. Liu, X. Sun, *et al.*, In-situ construction of hierarchical accordion-like TiO_2/Ti_3C_2 nanohybrid as anode material for lithium and sodium ion batteries, *Electrochim. Acta*, 2018, **271**, 165–172.

32 Z. Ma, X. Zhou, W. Deng, *et al.*, 3D porous MXene (Ti_3C_2)/reduced graphene oxide hybrid films for advanced lithium storage, *ACS Appl. Mater. Interfaces*, 2018, **10**(4), 3634–3643.

33 H. Huang, J. Cui, G. Liu, *et al.*, Carbon-coated $MoSe_2$/MXene Hybrid nanosheets for superior potassium storage, *ACS Nano*, 2019, **13**(3), 3448–3456.

34 Q. Zhao, Q. Zhu, J. Miao, *et al.*, Flexible 3D porous MXene foam for high performance lithium-ion batteries, *Small*, 2019, **15**(51), e1904293.